International Journal of Applied Earth Observations and Geoinformation 99 (2021) 102319

Contents lists available at ScienceDirect

International Journal of Applied Earth Observations and Geoinformation

journal homepage: www.elsevier.com/locate/jag

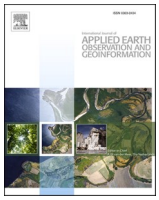

A method for predicting large-area missing observations in Landsat time series using spectral-temporal metrics

Zhipeng Tang *, Hari Adhikari, Petri K.E. Pellikka, Janne Heiskanen

Department of Geosciences and Geography, University of Helsinki, P.O. Box 68, FI-00014, Finland
Institute for Atmospheric and Earth System Research, Faculty of Science, University of Helsinki, Finland

ARTICLE INFO

Keywords:
Landsat
Remote sensing
Image reconstruction
Gap filling
k-Nearest Neighbor regression

ABSTRACT

Combined with increasing computing ability, the free and open access to Landsat archive has enabled the changes on the Earth's surface to be monitored for almost 50 years. However, due to missing observations that result from clouds, cloud shadows, and scan line corrector failure, the Landsat data record is neither a continuous nor consistent time series. We present a new gap-filling method, Missing Observation Prediction based on Spectral-Temporal Metrics (MOPSTM), which uses spectral-temporal metrics computed from Landsat one-year time series and the *k*-Nearest Neighbor (*k*-NN) regression. Herein, we demonstrate the performance of MOPSTM by using five, nearly cloud-free, full scene Landsat images from Kenya, Finland, Germany, the USA, and China. Cloud masks from the images with extensive cloud cover were used to simulate large-area gaps, with the highest value we tested being 92% of missing data. The gap-filling accuracy was assessed quantitatively considering all five sites and different land use/land cover types, and the MOPSTM algorithm performed better than the spectral-angle-mapper based spatiotemporal similarity (SAMSTS) gap-filling algorithm. The mean RMSE values of MOPSTM were 0.010, 0.012, 0.025, 0.012, and 0.018 for the five sites, while those of SAMSTS were 0.011, 0.017, 0.038, 0.014, and 0.023, respectively. Furthermore, MOPSTM had mean coefficient of determination (R^2) values of 0.90, 0.86, 0.78, 0.92, and 0.89, which were higher than those for SAMSTS (0.84, 0.75, 0.55, 0.89, and 0.83). The performance of MOPSTM was not considerably affected by image gap sizes as images ranging from gap sizes of 51% of the image all the way to 92% of the image yielded similar gap-filling accuracy. Also, MOPSTM does not require local parametertuning except for the *k* values in the *k*-NN regression, and it can make a gap-free image from any acquisition date. MOPSTM provides a new spectral-temporal approach to generate the gap-free imagery for typical Landsat applications, such as land use, land cover, and forest monitoring.

1. Introduction

Given the free availability of Landsat data since 1972 (Zhu et al., 2019), the interest in applications based on large-scale, multi-temporal Landsat data has continued to rise, especially for land cover classification (Knorn et al., 2009; Phiri and Morgenroth, 2017), land change monitoring (Zhu and Woodcock, 2014), and vegetation attribute modeling (Heiskanen et al., 2019; Wulder et al., 2019). Providing almost 50 years of Earth's surface records, Landsat acquires data at a spatial resolution of 30 m and temporal resolution of 16 days. However, a less attractive feature of Landsat data is missing observation – like with any other optical satellite data – which results from clouds and cloud shadows (CCS) (Chen et al., 2011; Gerber et al., 2018). Furthermore, the failure of the Landsat Enhanced Thematic Mapper Plus (ETM+) Scan Line Corrector (SLC) that occurred in May 2003 caused wedge-shaped gaps in each image thereafter, rendering roughly 22% of data unusable per image (Ju and Roy, 2008). Therefore, missing values continue to be a major barrier in applications of Landsat data.

Compositing procedures, image fusion (blending), and gap filling of individual images (i.e. interpolation or similar pixel replacement) are powerful tools for handling the missing observations in Landsat images (Gao et al., 2006; Zhu et al., 2010). Compositing procedures were developed to generate reflectance and vegetation index data for successive n-day periods (Yan and Roy, 2018). However, it is less reliable to apply compositing approaches to the Landsat data because the cloud-free observation frequency is lower than that provided by near-daily

* Corresponding author.
E-mail address: zhipeng.tang@helsinki.fi (Z. Tang).

https://doi.org/10.1016/j.jag.2021.102319
Received 26 May 2020; Received in revised form 14 January 2021; Accepted 25 February 2021
Available online 7 March 2021

coarse resolution satellite data (Griffiths et al., 2013; Roy et al., 2010; White et al., 2014; Yan and Roy, 2018). Image fusion (blending) uses coarser spatial resolution satellite data to fill missing information in the Landsat time series (Luo et al., 2018; Roy et al., 2008; Zhu et al., 2010), and it has been a popular approach among recent studies (Guo et al., 2020; Luo et al., 2018; Moreno-Martínez et al., 2020; Roy et al., 2008; Zhou and Zhong, 2020; Zhu et al., 2010). However, the complexity of the landscape and computational complexity can be challenges related to the method (Pohl and Van Genderen, 1998; Zhang, 2010).

Using valid observations from the same image or similar sensor for filling gaps is an alternative for compositing and blending (Vuolo et al., 2017; Yan and Roy, 2020; Yan and Roy, 2018). Shen et al. (2015) classified algorithms for reconstructing missing information into four categories: (1) spectral-based methods, (2) spatial-based methods, (3) temporal-based methods, and (4) hybrid methods. Spectral-based methods can simply recover the missing information by modeling the latent relationship between complete and incomplete spectral bands. They often aim to fill missing information caused by sensors where some bands are well recorded while others are not (Shen et al., 2015).

Spatial-based methods assume that the missing observations can be recovered from the remaining observations, which have similar spatial autocorrelation or geometrical structure. Interpolation methods that use non-missing neighboring observations to predict the missing observations, such as the geostatistical kriging technique (Zhang et al., 2007), belong to this category.

Temporal-based methods fill the gaps using the information from the data over the same geographical region but acquired at different time. Temporal replacement and filter methods belong to this category. The former one is a simple way to replace the gaps caused by CCS, but its weakness is possible difference in the brightness of pixels at different time due to the atmospheric conditions, the effects of sun and sensor-view angles, and the state of vegetation. For example, Chen et al. (2011) interpreted and replaced missing information in SLC-off images with the similar reflectance or close proximity from different dates. The latter one includes the adaptive Savitzky-Golay filter (Chen et al., 2004), asymmetric Gaussian (Jonsson and Eklundh, 2002), and Fourier transformation approaches (Brooks et al., 2012).

Hybrid methods include spatio-temporal and spectral-temporal methods. Cheng et al. (2014) used a pixel-offset based spatio-temporal Markov random fields global function to find a similar pixel in the uncontaminated regions. A geostatistical method improved the neighborhood similar pixel interpolator using geostatistical theory (Zhu et al., 2012). Malambo and Heatwole (2016) proposed a profile-based interpolator to recover missing information using a spatial window. Recently, Yan and Roy (2018) proposed a spectral-angle-mapper based spatio-temporal similarity (SAMSTS) method where gap pixels were filled by alternative similar pixels located in areas of non-missing observations. A spectral-angle-mapper metric was used to search alternative similar pixels and a time series segmentation-and-clustering approach was used to increase the searching efficiency.

There are only a few spectral-temporal methods proposed recovering missing information such as sparse-based reconstruction (Li et al., 2015) and patch-based reconstruction (Wu et al., 2018). Statistical spectral temporal metrics (STMs) are commonly used for land cover and vegetation attribute mapping (Adhikari et al., 2016; Potapov et al., 2012). Metrics, such as minimum, mean, maximum and different percentiles of spectral reflectance for a given temporal range provide effective representation of land surface spectral temporal characteristics. STMs can be calculated even when observations are only a few during a temporal range. In most cases, one year is an appropriate temporal range to calculate STMs as it covers complete vegetation growing cycle, has enough cloud-free observations per pixel, and is short enough for assuming that land use/land cover (LULC) changes are insignificant.

As gaps in STMs are rare (occur if there are no observations during a temporal range), STMs are considered to have potential for gap filling of individual images. However, this requires a machine learning method that is capable for identifying valid observations that have similar spectral temporal characteristics to the missing observations. As it is nonparametric and simple to undertake, the *k*-Nearest Neighbors (*k*-NN) method (Cover and Hart, 1967) has been widely used in many applications such as classification (Keller et al., 1985) and prediction of forest properties (Maltamo and Kangas, 1998). The *k*-NN regression has also been successfully used to predict missing information in various contexts (Beguería et al., 2019; Chiu et al., 2019; Poyatos et al., 2018) including remote sensing applications (Malambo and Heatwole, 2016).

Therefore, we propose a new gap-filling method based on STMs and *k*-NN regression and test its performance on large-area gaps of Landsat images over spatially heterogeneous and temporally dynamic regions. We refer to this method as Missing Observation Prediction based on Spectral Temporal Metrics (MOPSTM), and it incorporates two elements: (1) the computation of STMs, which include mean and percentiles derived from an annual Landsat time series and (2) the prediction of missing values based on STMs and the *k*-NN regression. The proposed MOPSTM algorithm was demonstrated using one year of Landsat 8 and 5 time series data. Five test areas in Kenya, Finland, Germany, the USA, and China were considered, which include various LULC types, such as forest, bushland, grassland, cropland, built-up areas, and water. Simulations of real CCS-shaped gaps removing different pixel areas were undertaken to provide insights into the gap-filling performance. The results were compared qualitatively and quantitatively with the SAMSTS gap-filling method which was recently published (Yan and Roy, 2018).

2. Material and methods

2.1. Study areas

We selected five study areas that each represented different ecosystems, land surface phenology, and topographic characteristics (Fig. 1). Site 1 is located in Taita Taveta County, Kenya (3°18′S, 38°30′E) where topography is variable, climate is moderate and humid, and terrain is hilly (Pellikka et al., 2018). Site 2 lies around Tampere, Finland (61°30′N, 23°46′E) with a flat topography, frequent cloud occurrence, and snow cover in winter. Site 3 is in Brandenburg, Germany (52°00′N, 13°24′E) where the area is covered by fragmented croplands. Site 4 is located in a topographic bowl in Maryland and Washington D.C. (38°40′N, 76°10′W) with the Potomac River running through the region. Finally, Site 5 is located in the Qinghai-Tibet Plateau (28°40′N, 89°10′E) and is surrounded by mountains with an average elevation exceeding 4,500 m. Also, there are six LULC types in the five sites: forest, bushland, grassland, cropland, built-up areas and water.

2.2. Gap-filling algorithm

2.2.1. Landsat images and pre-processing

The workflow of MOPSTM is summarized in Fig. 2. In order to test MOPSTM, nearly cloud-free images are used to simulate the gaps. Hereafter, we refer to any image that will be gap-filled as a target image. If applying the method, target images correspond to any image that needs to be filled. As nearly cloud-free images are rare, acquisition dates of target images vary from site to site. For the four sites, Landsat 8 target images were acquired from the following dates and years: March 9, 2017, August 21, 2015, October 12, 2018, and December 10, 2014, and one Landsat 5 image was acquired on September 13, 2007. We mainly used Landsat 8 Operational Land Imager (OLI) images but to check if the method works for the other Landsat sensor, we used Landsat 5 Thematic Mapper (TM) in one site.

The next step is to collect and pre-process Landsat time series datasets. We obtained Landsat Collection 1 Level-2 Surface Reflectance

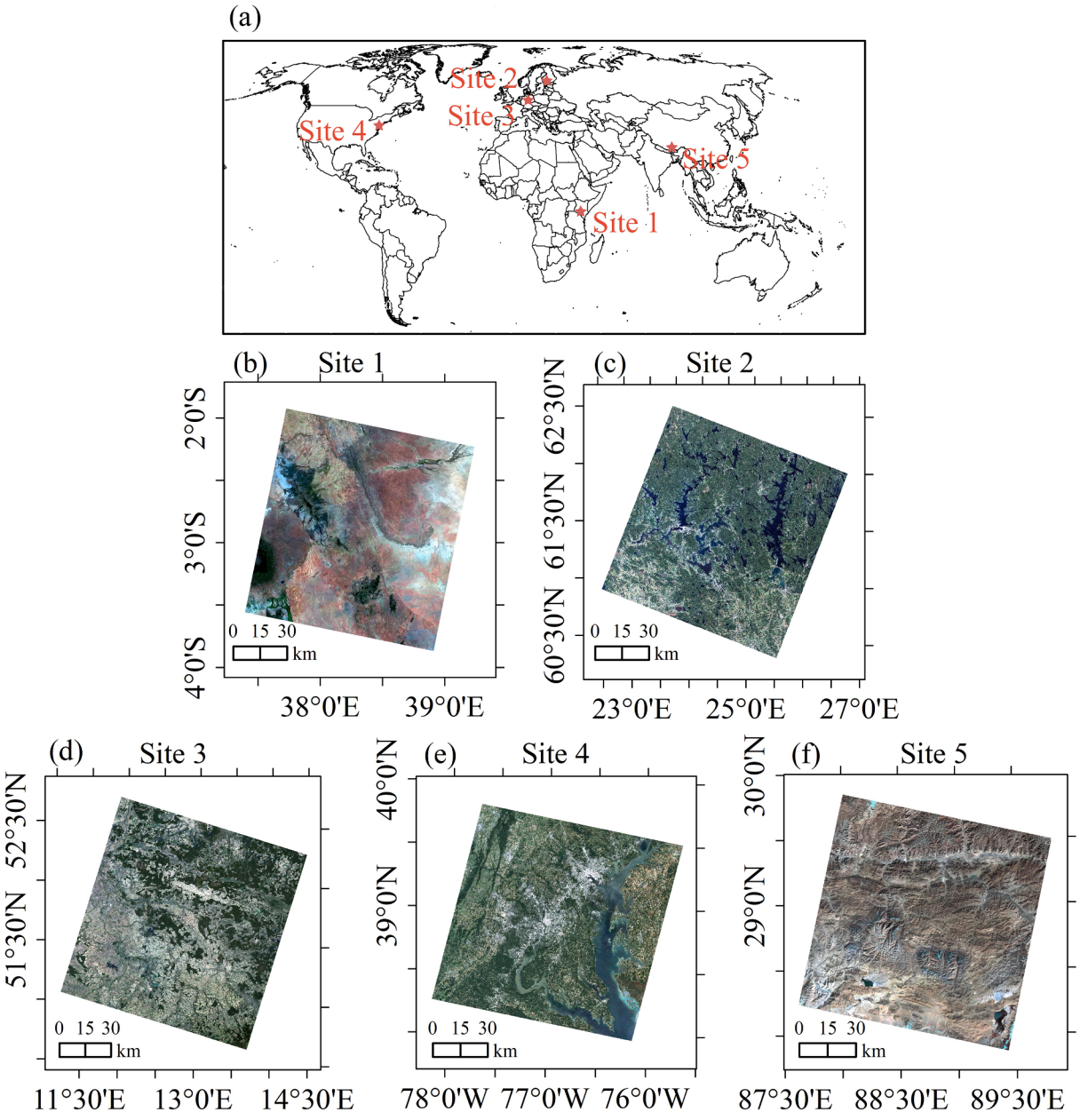

Fig. 1. (a) Locations of study areas, (b) Site 1: Taita Taveta County, Kenya, (c) Site 2: Tampere, Finland, (d) Site 3: Brandenburg, Germany, (e) Site 4: Maryland, USA, and (f) Site 5: Qinghai-Tibet Plateau, China.

products consisting of Landsat 8 OLI and Landsat 5 TM images for the five study areas from the USGS website[1]. The acquisition period for the time series was defined by the target image acquisition dates (Table 1). We preferred a temporal range that started six-months before and ended six-months after the target image acquisition time. For example, the target image in Site 1 was acquired on March 9, 2017, so the period starts in late August 2016 (about site months before) and ends in early September 2017 (about six months after). However, we adjusted the temporal range in Site 2, where the target image was acquired on August 21, 2015, based on the image availability because there were barely any observations collected from March to May in 2015. Therefore, we extended the temporal range to ten months after target image acquisition date (and two months before). Furthermore, in Site 3, November 2018 was the most recent date of images available when we started this work, so the temporal range was adjusted to start earlier than six months. An alternative for the temporal range selection would be to use calendar years for STM calculation.

Landsat Collection 1 Level-2 Surface Reflectance data were atmospherically corrected and derived from Level-1 data, which had systematic, radiometric, and geometric corrections using ground control points and a digital elevation model (Abdalati et al., 2010). Using "pixel quality" bands from CFMask cloud masks (Foga et al., 2017), we masked and removed pixels affected by CCS. The reflectance values were converted to a range from 0 to 1 (Chen et al., 2011). The numbers of images were 24, 9, 16, 15, and 23 in Sites 1–5, respectively and images covered completely by CCS were eliminated. Landsat 8 OLI images include seven bands [ultra blue, blue, green, red, near-infrared (NIR), and two shortwave infrared (SWIR1 and SWIR2)]. Landsat 5 TM images include six bands (excluding OLI ultra blue band).

[1] https://earthexplorer.usgs.gov/

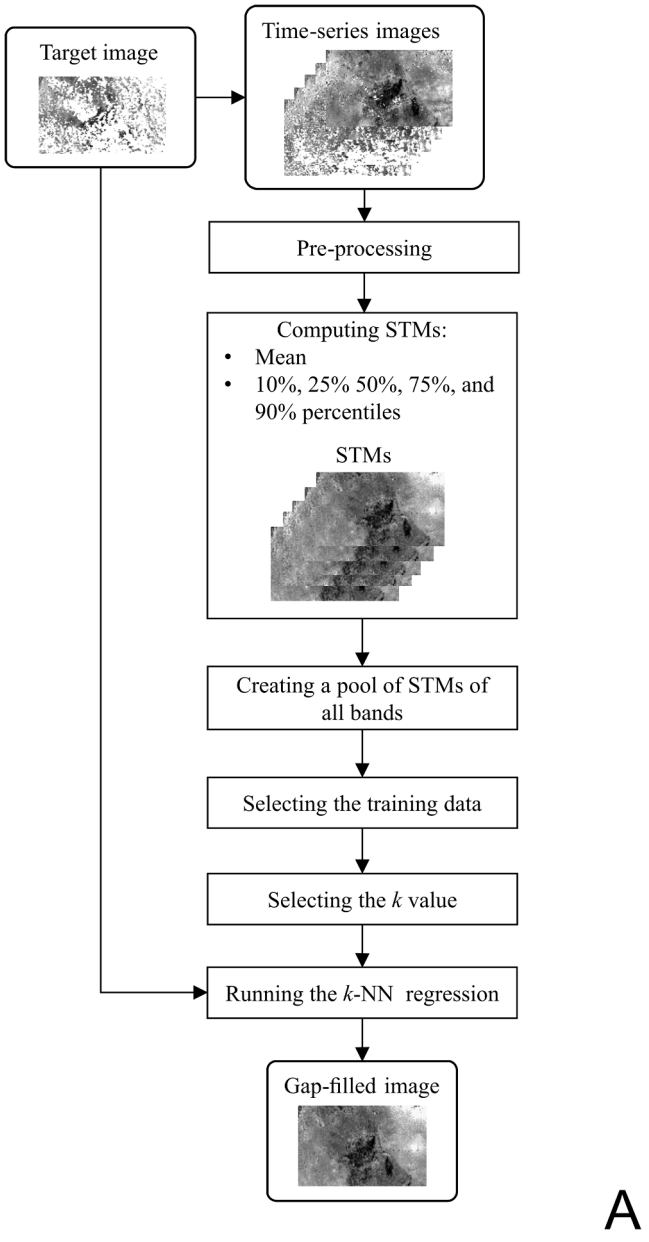

Fig. 2. Flowchart of the Missing Observation Prediction based on Spectral-Temporal Metrics (MOPSTM) method.

2.2.2. STMs computing

As STMs are derived from a one-year time series, the number of valid observations in one-year period can affect their quality. Therefore, we calculated the number of valid observations at each pixel location (Fig. 3). Site 5 in China had the largest number of valid observations with over fifteen valid observations in the majority of the area, and Site 1 in Kenya had the second largest number of valid observations where rather large areas also had over fifteen valid observations. However, there were relatively few valid observations in Site 2 in Finland, which had mostly under seven valid observations. This is explained by few observations during winter months.

After we computed STMs for each spectral band, we stacked them together to make a pool of STMs as the feature space for gap filling. With seven spectral bands used in Landsat 8 data, a pool of STMs contained 42 layers, and for Landsat 5, there were 36 layers. The median reflectance STMs are demonstrated in Fig. 4 where spatial texture and continuity are well presented.

2.2.3. The k-NN regression

In any target image, pixels with similar spectral temporal characteristics are likely to have similar reflectance. Based on this assumption, the *k*-NN regression is suitable to predict gaps in a target image using STMs as feature space.

For each site, we made a layer stack of STMs and a target image from where cloud-free pixels were sampled uniformly as a training dataset. A sensitivity test was conducted to test how the training dataset size affects the prediction accuracy. The number of training pixels varied from 10,000 to 80,000 in 5,000 pixel increments (Supplementary Fig. 1). Part of the target image was masked using a CCS mask, and training pixels were selected only from the cloud-free portion of the image. Then, accuracy was assessed using pixels that were masked but had reference reflectance (independent of training samples). The number of the test samples corresponded to the number of the gap pixels in each site and were the same for each training dataset size between 10,000 and 80,000. According to the sensitivity test (Supplementary Fig. 1), the increase of the training dataset size affected the root-mean-square error (RMSE) marginally. Therefore, we selected 20,000 pixels as a training dataset size.

There are two steps in the *k*-NN estimation procedure: selecting the *k* nearest or most similar samples and averaging the samples for the estimation. By establishing the relationship between non-missing pixel values in the same location in a target image and STMs, the *k*-NN regression can simply predict missing pixel values in the target image. Here, we used the *k*-NN method based on K-D Tree in the "FNN" package (Beygelzimer et al., 2015) in the R software environment (R Core Team 2018). We set Euclidean distance as a type of measurement to find the *k* nearest neighbors. To choose the *k* value, we optimized it by varying its value between 2 and 50 and checked how RMSE changed.

2.3. Simulated gaps based on cloud masks

We selected nearly CCS-free images as target images and simulated artificial large-area gaps using CCS-masks from other images. We computed the percentage of gaps for each image in the time series

Table 1
Landsat 5 Thematic Mapper (TM) and Landsat 8 Operational Land Imager (OLI) images.

Site	Location	Path and Row	Sensor	Number of bands	Area (km^2)	Spatial resolution (m)	Target image acquisition date	Time series temporal range	Number of images
Site 1	Taita, Kenya	167, 62	OLI	7	36,948	30	March 9, 2017	August 2016 – September 2017	24
Site 2	Tampere, Finland	189, 17	OLI	7	38,424	30	August 21, 2015	June 2015 – June 2016	9
Site 3	Brandenburg, Germany	193, 24	OLI	7	37,902	30	October 12, 2018	November 2017 – November 2018	16
Site 4	Maryland, USA	15, 33	TM	6	36,912	30	September 13, 2007	March 2007 – March 2008	15
Site 5	Tibet, China	139, 40	OLI	7	37,378	30	December 10, 2014	June 2014 – June 2015	23

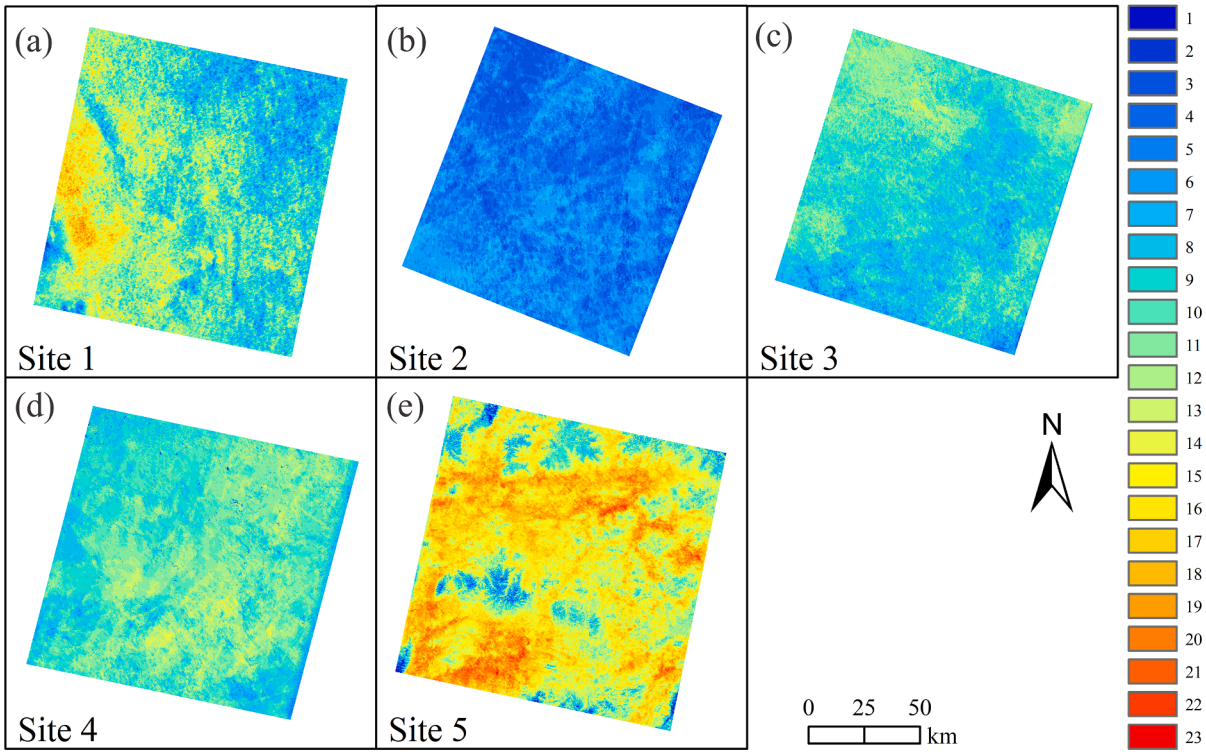

Fig. 3. Number of valid Landsat 5 and 8 observations at each 30 m pixel location for five sites: (a) Site 1, (b) Site 2, (c) Site 3, (d) Site 4, and (e) Site 5 over one-year period. Red color indicates more valid observations, and blue color indicates fewer valid observations. (For interpretation of the references to color in this figure legend, the reader is referred to the web version of this article.)

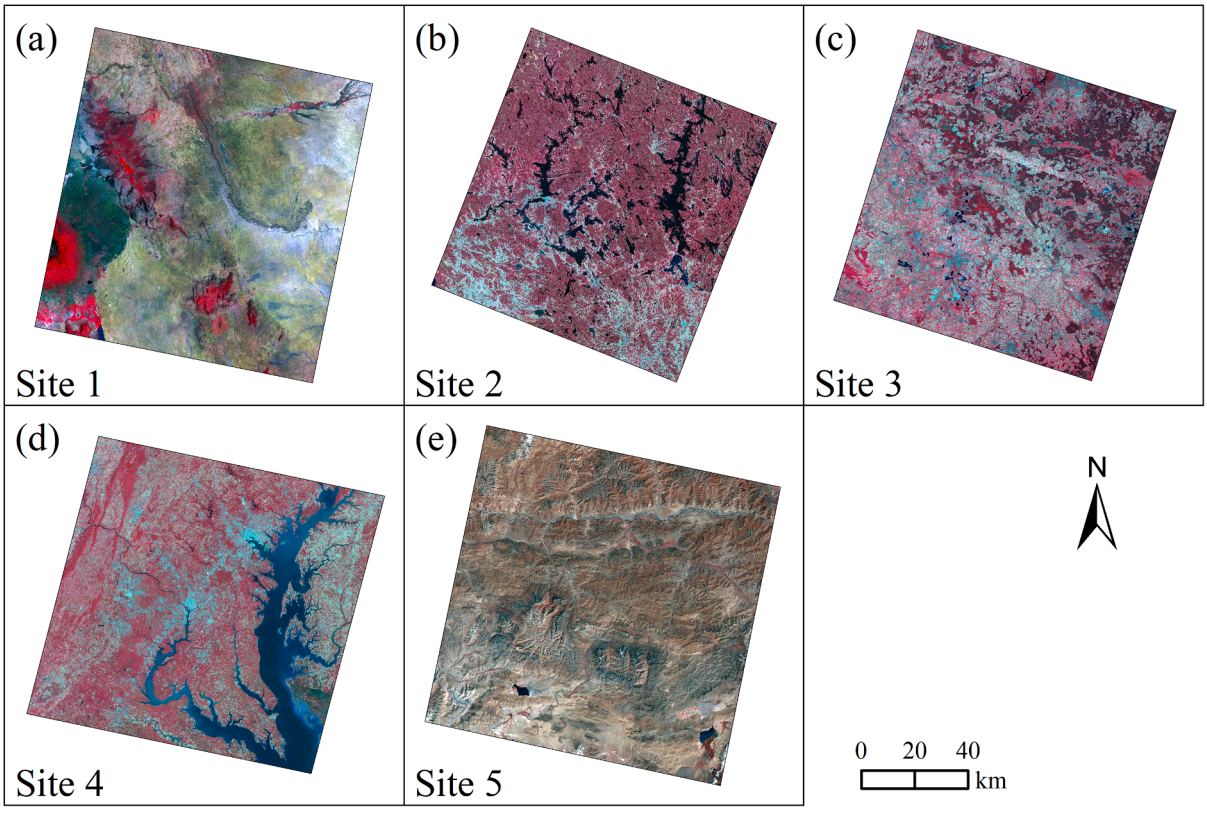

Fig. 4. The median reflectance of the Landsat time series over the five sites: (a) Site 1, (b) Site 2, (c) Site 3, (d) Site 4, and (e) Site 5 (false color composites of NIR, red and green bands). (For interpretation of the references to color in this figure legend, the reader is referred to the web version of this article.)

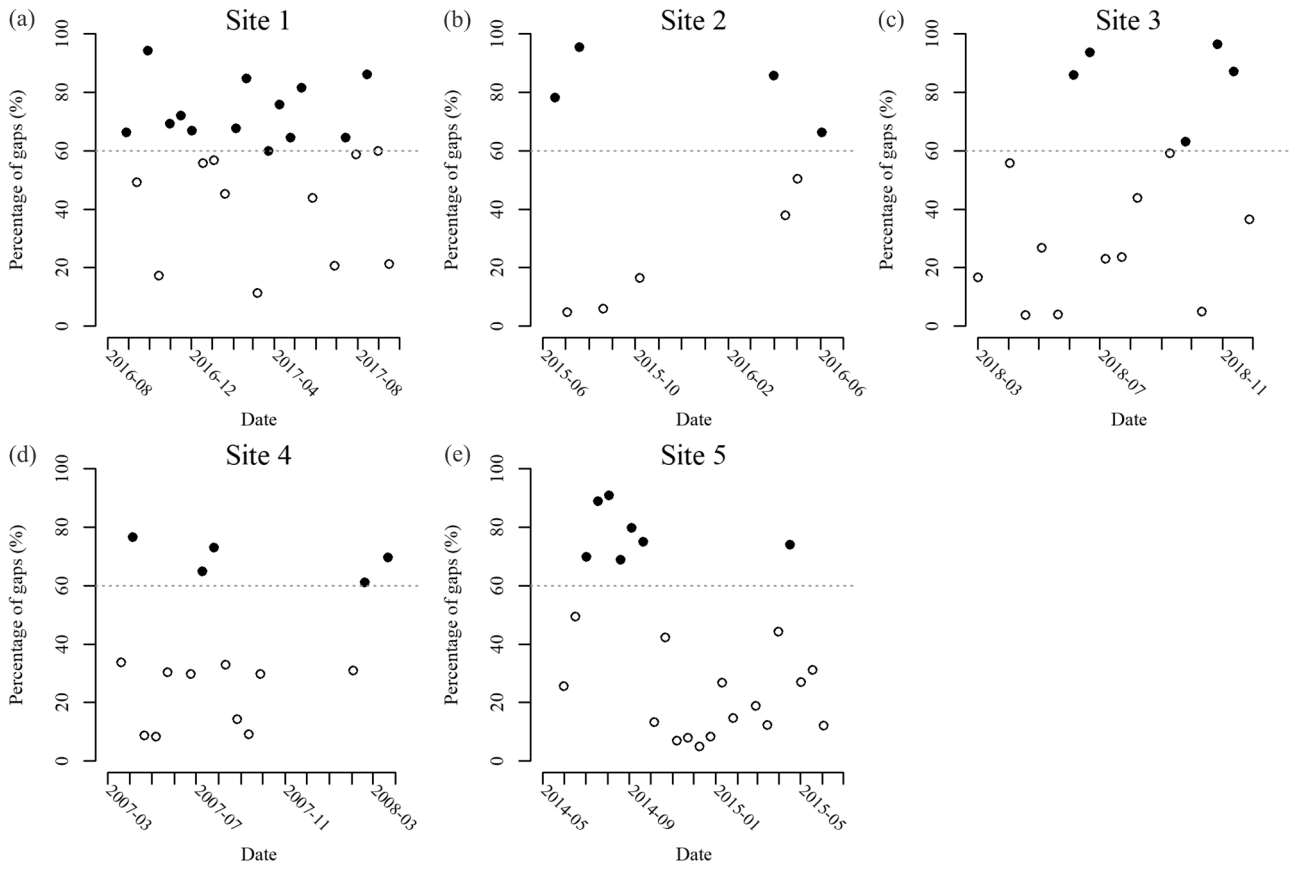

Fig. 5. The percentage of gaps in Landsat observations during a one-year period in the five study sites: (a) Site 1, (b) Site 2, (c) Site 3, (d) Site 4, and (e) Site 5. The horizontal dashed line shows the 60% level. The filled and unfilled circles have percentages ≥ 60% and < 60%, respectively. The percentages of filled circles in each site are 54%, 44%, 31%, 33%, and 30%, respectively. Scenes that have only clouds and cloud shadows are not shown.

(Fig. 5). Although there is no definition for which percentage of gaps is large, we considered 60% as a large level because over 30% of images in a one-year time series have gap areas over 60% (Fig. 5). As there were a number of images with a percentage of gaps over 80%, filling these images with the enormous area of gaps is also important. A majority of images in a one-year time series have a percentage of gaps <60%, so the performance of our method was evaluated by testing them, too. Thus, we grouped gaps into (1) < 60%, (2) 60–80%, and (3) > 80%.

Next, we selected CCS masks. The CCS masks derived from the images acquired from a closer date to the target images were preferred in order to simulate as realistic cloud patterns as possible. Three CCS masks were selected corresponding to the three groups of gaps, and we simulated CCS-shaped gaps in Sites 1–4, and a mixture shape of CCS and Landsat 7 SLC-off gaps in Site 5. The percentage of the simulated gaps for the five sites is shown in Fig. 6.

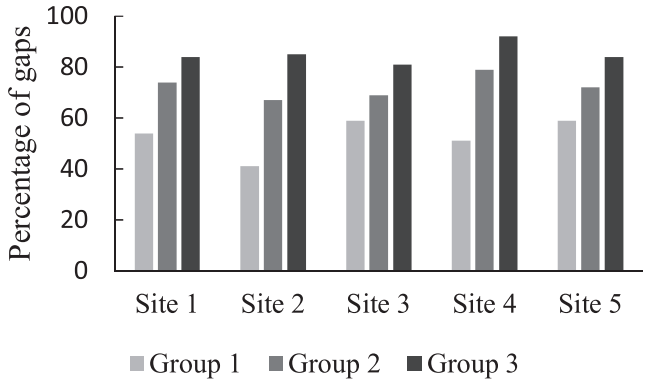

Fig. 6. Percentage of the simulated gaps for target images in five sites. The percentages of gaps in Groups 1–3 are < 60%, 60–80%, and > 80%, respectively.

2.4. Accuracy assessment and comparison to SAMSTS

We evaluated the performance of the MOPSTM gap-filling method both qualitatively and quantitatively. In terms of qualitative assessment, we assessed the spatial continuity of the gap filled pixels and the presence of noise visually. For the quantitative evaluation, the difference between the actual and predicted (gap-filled) data was derived as:

$$RMSE_{(i)} = \sqrt{\frac{\sum_{b=1}^{B} (\rho_s(x_i, y_i, b) - \widehat{\rho}_s(x_i, y_i, b))^2}{B}} \quad (1)$$

$$RMSE_{(b)} = \sqrt{\frac{\sum_{i=1}^{N}(\rho_s(x_i,y_i,b) - \hat{\rho}_s(x_i,y_i,b))^2}{N}} \quad (2)$$

$$R^2 = \frac{\sum_{i=1}^{N}(\rho_s(x_i,y_i,b) - \overline{\rho_s}(b))(\hat{\rho}_s(x_i,y_i,b) - \overline{\hat{\rho}_s}(b))}{\sqrt{\sum_{i=1}^{N}(\rho_s(x_i,y_i,b) - \overline{\rho_s}(b))^2 \sum_{i=1}^{N}(\hat{\rho}_s(x_i,y_i,b) - \overline{\hat{\rho}_s}(b))^2}} \quad (3)$$

where $RMSE_{(i)}$ is the total band root-mean-square error for pixel i, $RMSE_{(b)}$ is the root mean square error for band b, R^2 is the coefficient of determination for each band, N is the number of total pixels, B is the total number of bands, $\rho_s(x_i,y_i,b)$ and $\hat{\rho}_s(x_i,y_i,b)$ are the actual and predicted values of the ith pixel in band b, respectively, $\overline{\rho_s}(b)$ and $\overline{\hat{\rho}_s}(b)$ are the average values of $\rho_s(x_i,y_i,b)$ and $\hat{\rho}_s(x_i,y_i,b)$ in band b, respectively. For the five sites, the RMSE and R^2 results were assessed using all the simulated gap pixels, which are independent to the training datasets.

We assessed whether the accuracy of the gap-filling method differed in LULC types. For Site 1, we downloaded "S2 prototype LC map at 20 m of Africa 2016" from the ESA CCI LC 2016[2]. For Site 2 and Site 3, we downloaded "Corine Land Cover (CLC) 2018" from the Copernicus Global Land Service website[3]. For Site 4, we downloaded "USGS National Land Cover Database (NLCD) 2011" from the U.S. Geological Survey (USGS) website[4]. For Site 5, we downloaded global land cover map for the 2010 epoch from the website of ESA Climate Change Initiative[5]. Then, we reclassified LULC types into forest, bushland, grassland, cropland, built-up areas, and water and assessed accuracy separately for each type.

Finally, the MOPSTM performance was compared with the SAMSTS algorithm (Yan and Roy, 2018), which can also predict large-area gaps in time series. To reduce the computing time, the SAMSTS method was applied to subsets of the full scene images to predict gaps. To test whether the algorithm is robust to different sizes of images, we made various subsets in the five sites: about 3000 × 3000 pixels subset with 63% of gaps for Site 1, about 2000 × 2000 pixels subset with 61%, 85%, and 74% of gaps for Sites 2, 3 and 5, respectively, and about 4000 × 4000 pixels subset with 42% of gaps for Site 4. Both SAMSTS and MOPSTM were applied to the Landsat time series separately to predict reflectance in the seven Landsat 8 bands and six Landsat 5 bands.

3. Results

3.1. Optimization of the k value

Using MOPSTM, the only parameter that needed to be set was the k values – the number of k nearest neighbors in the k-NN regression. In order to test how accuracy depends on k, we optimized its value by varying k in the range of 2–50 (Fig. 7). We tested simulated gaps for Sites 1–5, respectively. For saving computing time, approximately 30% of the pixels in full-scene images were tested.

As it is difficult to select an optimal k value for all sites, the mean RMSE of the five sites was calculated to assist deciding it. In Fig. 7, the highest accuracy occurred when k ranged from 6 to 16. Smaller and larger values decreased accuracy, except in Site 3 where higher values of k had a relatively small effect. Noticing that the k values between 6 and 16 did not make RMSE difference over 0.001, we selected 10 as a value of k and applied it to all five sites because it had the lowest mean RMSE value across all the sites (green line in Fig. 7). If focusing only on one site, further optimization of k is advised.

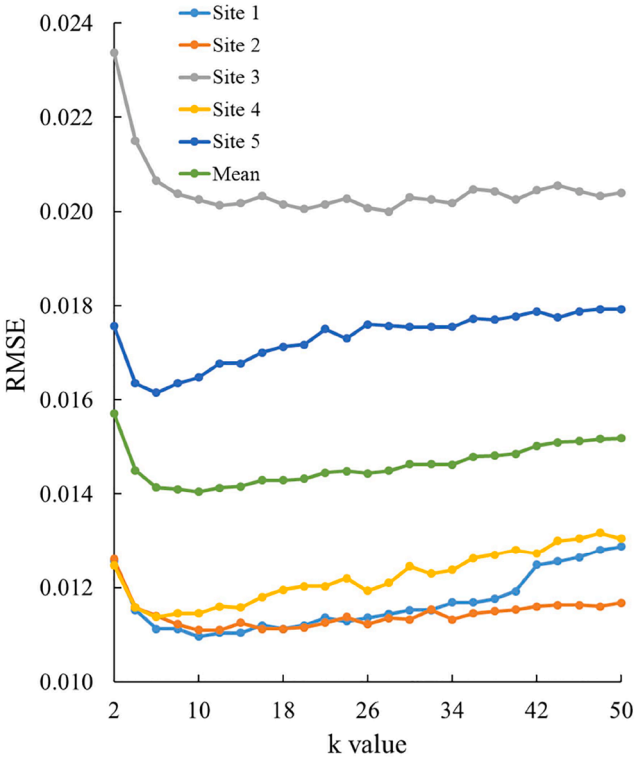

Fig. 7. The mean RMSE of the gap-filling results of all bands when using different k values.

3.2. Quantitative validation

3.2.1. Accuracy of the full scene images

The results of the MOPSTM gap-filled images with simulated CCS masks are shown in Fig. 8. The target images with simulated gaps can be seen in Fig. 8a. The gaps correspond to the CCS masks in Sites 1–4. Site 5 also included Landsat 7 SLC-off gaps. Fig. 8b showed the actual images, which are nearly gap-free, except in Site 1. Gap-filled images are in Fig. 8c, and it is apparent that all the gap-filled images are similar to the actual image without obvious errors. In Fig. 8d, residuals between the actual and gap-filled pixels indicate a good pixel-wise performance. Most of the residuals were between −0.06 and 0.06, and Site 2 turned out to have the smallest pixel level error. The other filled results for various simulated gaps are shown in Supplementary Fig. 2.

The dependence of the accuracy on the percentages of gaps is shown in Fig. 9. The results indicate different percentages caused small effects on gap-filling performance. For example, in Site 1, 84% and 53% of gaps yielded similar RMSE and R^2 values of about 0.010 and 0.88, respectively. In Site 3, 80% and 60% of gaps yielded identical RMSE and R^2 values of around 0.025 and 0.77, respectively.

The relationship between the actual and predicted reflectance values for seven bands in Site 1 are shown in Fig. 10. The scatterplots for the other four sites are shown in the Supplementary Fig. 3. A high density of points fell close to the 1:1 line in each band while some points deviate further from the line. The agreement between actual and predicted values was the best for the blue band (Fig. 10b) with the smallest RMSE value (0.004) and a high R^2 value (>0.90) in Fig. 10 while the NIR band (Fig. 10e) had the largest RMSE and the smallest R^2, which may be because the NIR band was more sensitive to vegetation coverage that could vary in reflectance during the year. Also, the two SWIR bands (Fig. 10f and 10g) had a good prediction accuracy with RMSE values under 0.020 in Sites 1, 2, and 4.

[2] http://2016africalandcover20m.esrin.esa.int/
[3] https://land.copernicus.eu/pan-european/corine-land-cover/clc2018
[4] https://www.mrlc.gov/data/nlcd-2011-land-cover-conus-0
[5] http://cci.esa.int/content/land-cover-data

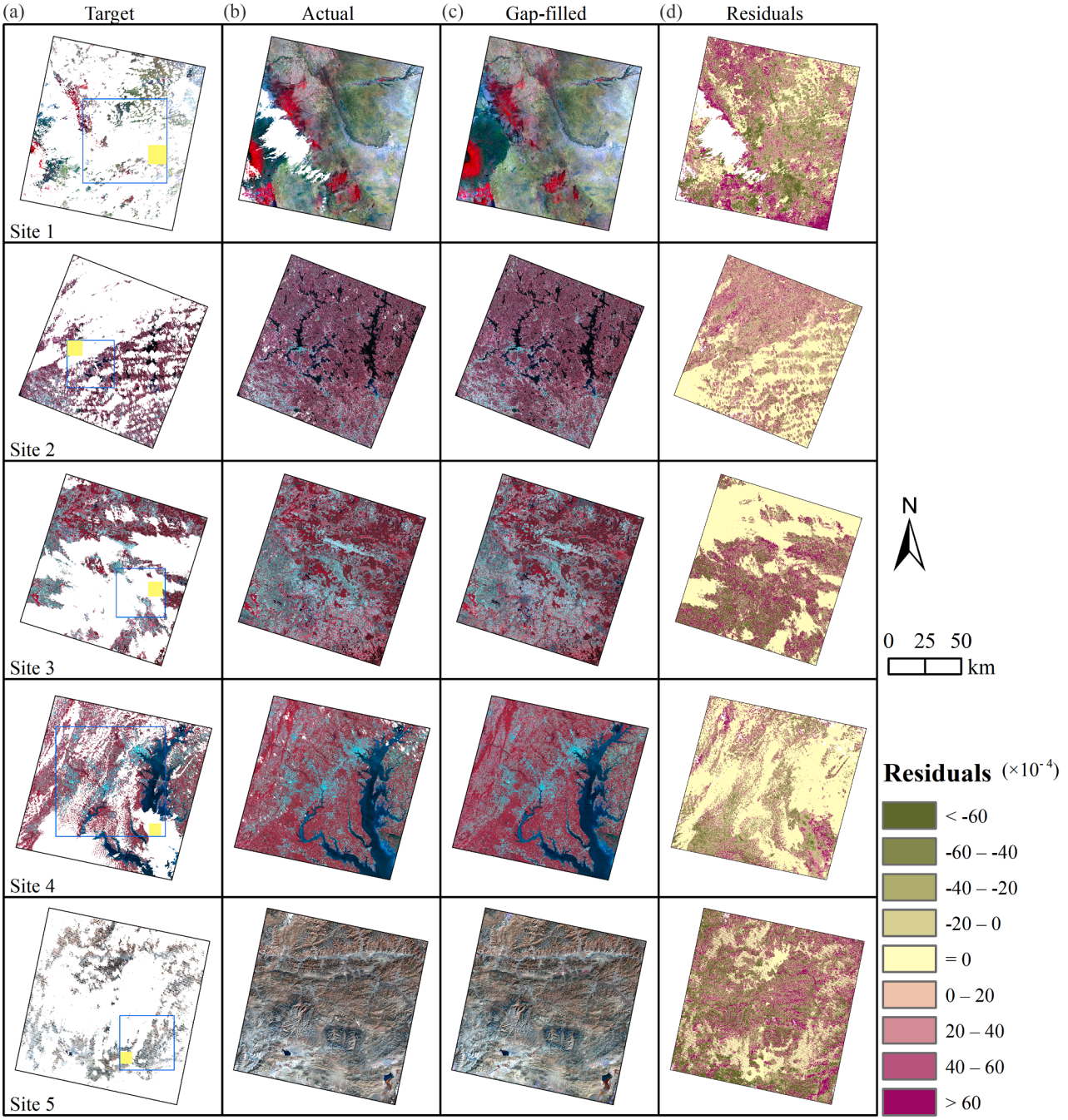

Fig. 8. Examples of the MOPSTM gap-filling results with residuals (actual – gap-filled) for full scene images over the five sites (false color composites of NIR, red and green bands), acquired on March 9, 2017, August 21, 2015, October 12, 2018, September 13, 2007, and December 10, 2014, respectively. (a) Target image, (b) actual image, (c) gap-filled image, and (d) residual image. The numbers of cloud-free pixels were 6,532,961 in Site 1 (in total 41,053,814), 14,073,787 in Site 2 (in total 42,693,097), 16,775,954 in Site 3 (in total 42,113,624), 20,287,589 in Site 4 (in total 41,013,201), and 6,538,444 in Site 5 (in total 41,530,738). The percentages of simulated gaps were 84% in Site 1, 67% in Site 2, 60% in Site 3, 51% in Site 4 and 84% in Site 5. The blue frames in the target images indicate the subset results in Table 2 and the yellow squares indicate the smaller subset results shown in Fig. 11. (For interpretation of the references to color in this figure legend, the reader is referred to the web version of this article.)

3.2.2. *Comparison with SAMSTS*

In order to quantitatively compare the MOPSTM and SAMSTS gap-filling (results are shown in Supplementary Fig. 4) algorithm performance, mean RMSE (Eq. (2)) and R^2 for seven bands from Landsat 8 and six bands from Landsat 5 were computed for subsets in the five sites (Table 2). Larger RMSE and smaller R^2 values were observed for the SAMSTS in all five sites. SAMSTS predicted the best in Site 1 with RMSE of 0.011, which was a little larger than RMSE for MOPSTM (0.010). However, SAMSTS predicted the worst in Site 3 with RMSE of 0.038, which was much larger than RMSE for MOPSTM (0.025). In Site 3, R^2 for SAMSTS was only 0.55, but it was 0.78 for MOPSTS, which was the largest difference between these two methods in any site.

The results for the smaller subsets (between 400 × 400 and 600 × 600 pixels, see yellow squares in Fig. 8 for subset locations) are shown in Fig. 11 and Supplementary Figs. 5–8, where SAMSTS and MOPSTM gap-filling results are compared with the actual images on pixel-wise RMSE evaluations. This comparison illustrates that the gap-filling using SAMSTS (Fig. 11a) is less accurate than using MOPSTM (Fig. 11b); the

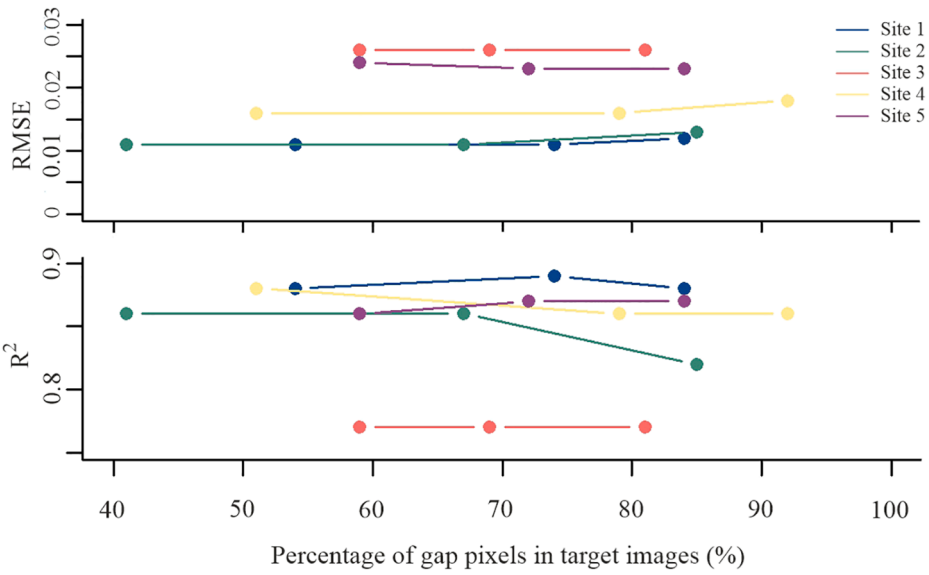

Fig. 9. The dependence of the MOPSTM gap-filling accuracy for full scene images on the fraction of gaps over the five sites.

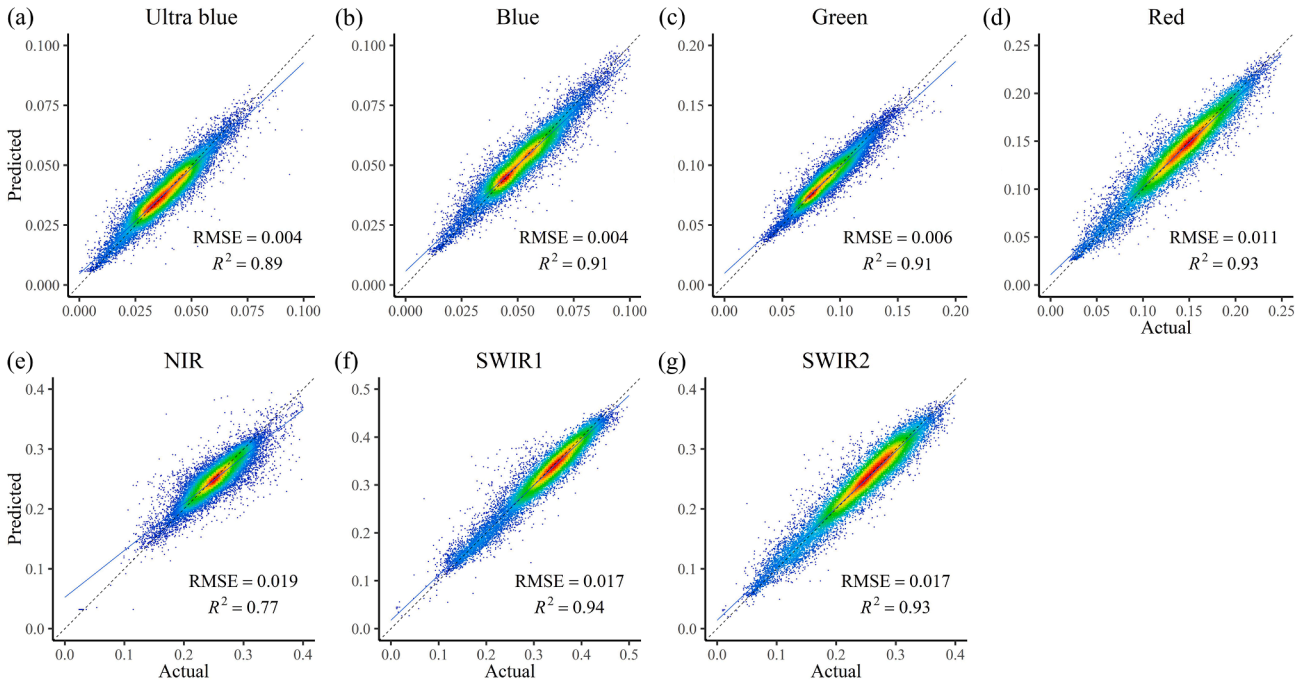

Fig. 10. Density scatter plot of the relationship between the actual and MOPSTM predicted (gap-filled) reflectance in different spectral bands: (a) ultra blue, (b) blue, (c) green, (d) red, (e) near-infrared (NIR), (f) and (g) two shortwave infrared (SWIR1 and SWIR2) bands in the full scene target image with 84% of gaps in Site 1. The black dashed line is the 1:1 line and the solid line shows the linear regression fits. Red color indicates higher density of points and blue color indicates lower density of points. (For interpretation of the references to color in this figure legend, the reader is referred to the web version of this article.)

Table 2
Comparison of SAMSTS and MOPSTM performance: mean RMSE (Eq. (2)) and R^2 for seven bands of Landsat 8 and six bands of Landsat 5 over the subsets in five sites (see blue frames in Fig. 8 for subset locations).

Site	Area (km^2)	Percentage of gaps (%)	SAMSTS		MOPSTM	
			RMSE	R^2	RMSE	R^2
Site 1	8,710	63	0.011	0.84	0.010	0.90
Site 2	3,600	61	0.017	0.75	0.012	0.86
Site 3	3,600	85	0.038	0.55	0.025	0.78
Site 4	15,300	42	0.014	0.89	0.012	0.92
Site 5	3,600	74	0.023	0.83	0.018	0.89

gaps that were filled by SAMSTS were sometimes spatially incoherent with obvious gap-filling errors observed as high RMSE values. In contrast, the gap-filled images provided by MOPSTM had a more natural look. The majority of the MOPSTM RMSE values (Fig. 11e) were smaller than the corresponding SAMSTS RMSE values (Fig. 11d, 51%, 66%, 73%, 73% and 55% of the pixels for Sites 1–5, respectively).

To compare the performance of MOPSTM and SAMSTS for different LULC types, the subset results (blue frames in Fig. 8) were further disaggregated based on LULC data. The mean normalized RMSE and R^2 of all Landsat bands using SAMSTS and MOPSTM gap-filling methods for each LULC type are presented in Table 3. We found that SAMSTS normalized RMSE values were 0.3% and 0.9% lower and SAMSTS R^2

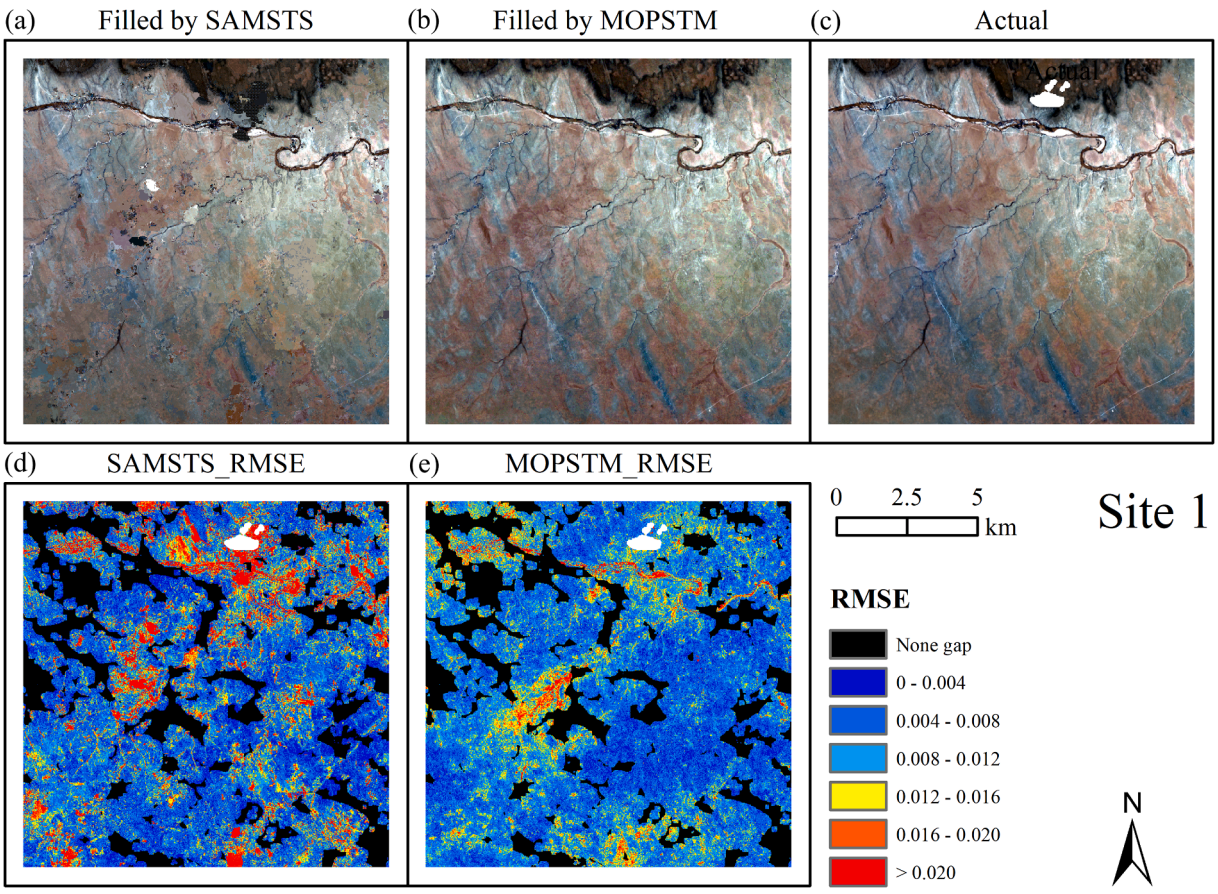

Fig. 11. A comparison of SAMSTS and MOPSTM results for the smaller subset of Site 1 shown in Fig. 8 (false color composites of NIR, red, and green bands): a river, mountain area and bushland. (a) Gap-filled image using SAMSTS, (b) gap-filled image using MOPSTM, (c) actual image (original Landsat image), (d) SAMSTS RMSE, and (e) MOPSTM RMSE. RMSE (Eq. (1)) was computed for the predicted reflectance values and the observed reflectance values in the seven bands of Landsat 8. Pixels with no gap in the actual image are shown in black. (For interpretation of the references to color in this figure legend, the reader is referred to the web version of this article.)

values were 0.05 and 0.02 higher than those of MOPSTM from cropland in Sites 4 and 5, which took up only 3.8% and 0.1% of the whole area. Aside from this, all other normalized RMSE and R^2 values indicated that MOPSTM performed better than SAMSTS in any LULC types from all five sites, with a largest difference of normalized RMSE of 28.9% in forest and R^2 of 0.47 in bushland in Site 3.

4. Discussion

Either insufficient cloud-free reference images or the difficulty of finding alternative similar pixels in relatively small spatial windows has limited the use of current gap-filling methods (Chen et al., 2011; Malambo and Heatwole, 2016; Yan and Roy, 2018). These constraints are decreased by the method presented in this study, where the large-area gaps were filled using STMs based on time series imagery and non-parametric *k*-NN regression.

Methods that can fill large-area gaps in the full scene Landsat images are scarce. Compared with SAMSTS (Yan and Roy, 2018) in all five sites, MOPSTM had a smaller mean RMSE value and a larger mean R^2 value for all spectral bands. In terms of LULC types, MOPSTM performed better than SAMSTS in each type except for cropland in Sites 4 and 5 where MOPSTM had a marginally lower accuracy. This may be because local-scale cropland management caused a temporal variation in reflectance throughout the year so that reflectance differed between the target image and other images in time series. That also explains why Site 3 was most poorly predicted as 80% of Site 3 is made up of fragmented cropland. Overall, the MOPSTM method performed the best in forest, bushland, and grassland such as in Site 1 where bushland and grassland were predicted most accurately. The reason may be that bushland and grassland are semi-natural vegetation in the area and relatively homogenous across the scene, which means that similar pixels are more likely predicted. It is also worth noting that built-up areas in Site 4 had very low RMSE and very high R^2 values, which proves that MOPSTM works well in spectrally heterogeneous regions such as urban areas.

In addition to higher accuracy, MOPSTM has obvious advantages over SAMSTS. First, MOPSTM is simpler to conduct and does not require parameter tuning except *k* in the *k*-NN regression. The segmentation process in SAMSTS produced unwanted noise (e.g. in the water area of Site 4 and in the mountains of Site 5). Second, MOPSTM can fill gaps that account for up to 92% of an image. SAMSTS is less reliable in filling the enormous area of gaps (e.g., over 80%). For example, SAMSTS had RMSE of 0.038 and R^2 of 0.55 for filling gaps up to 85% in the subset of Site 3 and was much less accurate than MOPSTM (RMSE of 0.025 and R^2 of 0.78). For the full scene images gap-filled by MOPSTM, we noted that as the area of the gaps increased, the accuracy remained nearly the same, meaning that MOPSTM performs robustly even when a very large fraction of the image is missing.

The MOPSTM gap-filling method took from 7.6 to 12 h to process a single full scene image (seven or six bands) on an Intel Core i5-7200 CPU @ 2.50 GHz processor. This is much shorter than the method proposed by Vuolo et al. (2017) with 30-core hours using 1000 templates based on an Intel Core i7-2600 K @ 3.40 GHz processor. The SAMSTS gap-filling method took over 18 h to process a stack of time series images with 5000 × 5000 30 m pixels and 60 bands. The computing time of MOPSTM

Table 3
Overview of the mean normalized RMSE (Normalized $RMSE_{(b)} = RMSE_{(b)}/mean(\rho_s(b)), \rho_s(b)$ is the spectral reflectance of band b) and R^2 (Eq. (3)) values grouped by land use/land cover types using SAMSTS and MOPSTM in the five sites. The Area is the percentage of each type. The highest and lowest values are presented in bold (see blue frames in Fig. 8 for subset locations).

	LULC types	Site 1			Site 2			Site 3			Site 4			Site 5		
		Area (%)	SAMSTS	MOPSTM	Area (%)	SAMSTS	MOPSTM	Area (%)	SAMSTS	MOPSTM	Area (%)	SAMSTS	MOPSTM	Area (%)	SAMSTS	MOPSTM
Normalized RMSE (%)	Forest	1.4	10.3	9.6	14.2	24.2	16.6	6.6	44.7	**15.8**	5.7	15.6	13.2	0.4	**15.7**	15.5
	Bushland	46.4	**7.0**	**6.1**	1.9	28.5	18.7	0.4	48.5	22.2	22.7	16.2	14.2	1.7	21.1	15.9
	Grassland	26.3	8.6	7.0	3.9	**23.3**	**16.3**	1.1	33.3	16.0	9.2	15.0	12.9	76.4	16.0	12.5
	Cropland	25.2	10.0	8.7	28.5	36.8	27.4	80.0	**30.1**	20.6	3.8	19.3	**19.6**	0.1	**22.0**	**22.9**
	Built-up areas	0.3	**16.1**	9.5	15.6	29.6	22.6	11.0	37.8	20.8	19.4	**13.3**	**10.3**	10.6	16.9	**11.0**
	Water	0.4	14.6	**9.7**	35.9	**53.5**	**34.0**	0.9	**80.9**	**61.5**	39.2	**20.7**	16.6	10.8	19.5	15.6
R^2	Forest	1.4	0.81	0.86	14.2	0.72	**0.87**	6.6	0.39	0.82	5.7	0.84	0.87	0.4	0.81	0.81
	Bushland	46.4	0.83	0.89	1.9	0.65	0.84	0.4	0.40	**0.87**	22.7	0.82	0.84	1.7	0.75	0.86
	Grassland	26.3	**0.86**	**0.92**	3.9	0.69	0.84	1.1	**0.43**	0.82	9.2	0.80	0.85	76.4	**0.83**	**0.90**
	Cropland	25.2	0.72	**0.81**	28.5	**0.33**	**0.55**	80.0	**0.31**	**0.59**	3.8	**0.74**	**0.69**	0.1	**0.70**	**0.68**
	Built-up areas	0.3	**0.68**	0.89	15.6	**0.77**	0.86	11.0	0.39	0.76	19.4	**0.90**	0.93	10.6	0.78	**0.90**
	Water	0.4	0.71	0.87	35.9	0.72	0.83	0.9	0.37	**0.59**	39.2	**0.90**	**0.94**	10.8	0.79	0.86

is still long, for example, for filling all the images in the one-year time series, but can be reduced considerably if processing smaller areas than full scenes. Furthermore, the full time series also includes images that have fewer missing observations, and hence, are faster to process.

The disadvantage of MOPSTM is that it is unable to provide the uncertainty of the prediction, which geostatistical approaches can do (Zhu et al., 2012). However, Supplementary Fig. 9 shows the Euclidean distance of each gap pixel to a nearest pixel in the training dataset in the feature space, which provided a way to evaluate the uncertainty. Basically, the shorter the spectral distance between the target and nearest pixel was, the more accurate the predictions were. Although most of the sites had relatively short distances to the nearest neighbors, some regions had relatively long distances such as the center areas in Site 5, which is more likely to cause uncertainty in predicting gaps. However, there is no indication that large-area gaps increased uncertainty caused by the nearest neighbor distance as the Site 1 with 84% of gaps did not have more large distance areas than other sites with smaller percentages of gaps.

Apart from the distance to the nearest neighbors, the spatial coverage of the training dataset may also cause the predicting uncertainty. When CCS cover a specific LULC type, there are no specific pixels for that LULC type available in the training dataset for filling. This situation rarely happens if LULC types are abundant across the image. For example, we showed a scatter plot of the NIR band reflectance versus the red band reflectance in Supplementary Fig. 10, in which 20,000 pixels covered the feature space well in most of the sites, although some parts of the feature space without observations can also be identified. However, if this is a serious problem, gap-filling could be attempted in that case for a mosaic of images with better availability of LULC types.

Another potential issue with MOPSTM is the lack of valid observations for calculating STMs. If observations are completely missing, MOPSTM cannot predict gaps; if observations are significantly missing, MOPSTM might be negatively affected. In Site 2, the number of valid images collected during one year was nine, which corresponds to the Finnish site with few images during winter. However, nine images provided adequate temporal information for calculating, for example, mean reflectance for gap-filling purposes. This demonstrates that in some sites the temporal range for calculating STMs can be shorter than one year (e.g. from spring to autumn only).

In addition, the temporal range is a sensitive factor in time series processing because changes occur during the period (Shen et al., 2015). Two types of changes occur within one year: 1) seasonal variation of reflectance and 2) long term changes in LULC types. As category one changes are dominant, category two changes are usually limited in area within one year. Our method can deal with seasonal variations as it uses pixels from the same image to fill gaps. Furthermore, STMs can be used for filling gaps in images acquired in different seasons. The category two is not taken into account as STMs are calculated using one year of data. In these cases, STMs include data from both periods (before and after changes happen) and can be noisy. Therefore, gap-filling results of those pixels can be unpredictable; however, LULC changes are typically observed in longer time scales instead of over periods shorter than one year.

In principle, MOPSTM is applicable to data from other multispectral sensors that are able to collect time series of imagery for calculating STMs, such as Sentinel-2. As time series of imagery is required, free imagery is the most viable option. Lower resolution sensors that provide much denser temporal sampling, such as MODIS and other options which are bi-monthly or monthly composites, are more appropriate. MOPSTM also has the potential to be combined with other methods, including image compositing. In cloud-prone areas, gap-filling can be an option to derive an observation that better matches the desired season for image compositing (e.g. peak of the growing season), rather than the closest valid observation in time. Furthermore, Yan and Roy (2018) combined gap-filling with curve fitting, which enables the prediction of Landsat image for any day of the year. MOPSTM provides a simple

alternative for gap-filling part of such an approach.

The further studies of MOPSTM can be testing how gap-filled images perform for LULC classification in comparison to real observations. Furthermore, since image fusion methods such as the spatial and temporal adaptive reflectance fusion model (STARFM) (Gao et al., 2006) are very different from MOPSTM, it would be also interesting to compare the strengths and weakness of both methods as well as other alternative methods. Due to the successful application of machine learning based image processing, the comparison of data reconstructing methods related to different machine learning methods (e.g. Markov random fields (Cheng et al., 2014), *k*-NN (Beguería et al., 2019; Malambo and Heatwole 2016), and neural networks (Xing et al., 2017)) are also interesting. A review of comparing all the approaches with the same data would be beneficial as a topic for further study.

5. Conclusion

We presented a novel algorithm Missing Observation Prediction based on Spectral-Temporal Metrics (MOPSTM) for Landsat reflectance time series over one year. The MOPSTM method uses spectral-temporal metrics to fill large-area gaps in Landsat images based on the *k*-NN regression. To evaluate the performance of MOPSTM, five sites with strong seasonal reflectance variations in Kenya, Finland, Germany, the USA, and China, were tested.

We simulated large-area gaps that were comparable to the actual variations in cloud and cloud shadow cover in Landsat data. MOPSTM proved to be capable of filling gaps covering as much as 92% of the image with accuracy similar to lower gap percentages. This demonstrates that MOPSTM works efficiently even when a very large fraction of the image is missing.

The MOPSTM method performed better than SAMSTS, and it offers several advantages, including the fact that it does not require local parameter tuning except for *k* in the *k*-NN regression. Future studies should test MOPSTM as a part of their time series pre-processing, as well as image analysis workflows such as vegetation attribute modelling, LULC classification, and change monitoring.

CRediT authorship contribution statement

Zhipeng Tang: Conceptualization, Methodology, Data curation, Writing - original draft, Validation, Writing - review & editing, Funding acquisition. **Hari Adhikari:** Data curation, Writing - review & editing. **Petri K.E. Pellikka:** Writing - review & editing, Supervision, Funding acquisition. **Janne Heiskanen:** Conceptualization, Methodology, Writing - review & editing, Supervision.

Declaration of Competing Interest

The authors declare that they have no known competing financial interests or personal relationships that could have appeared to influence the work reported in this paper.

Acknowledgments

The study was funded by the China Scholarship Council fellowship (, I am kind of confused Funding NO. 201706040079). Petri Pellikka acknowledges funding from the Academy of Finland for the SMARTLAND project (decision number 318645). We thank Dr. Giuseppe Amatulli for his comments on the manuscript, Dr. Lin Yan for debugging his script of the SAMSTS algorithm, and Mr. Clayton Snider for revising the language. We also appreciate the comments by the anonymous reviewers and journal editor.

Appendix A. Supplementary material

Supplementary data to this article can be found online at https://doi.org/10.1016/j.jag.2021.102319.

References

Abdalati, W., Zwally, H.J., Bindschadler, R., Csatho, B., Farrell, S.L., Fricker, H.A., Harding, D., Kwok, R., Lefsky, M., Markus, T., 2010. The ICESat-2 laser altimetry mission. Proc. IEEE 98, 735–751.

Adhikari, H., Heiskanen, J., Maeda, E.E., Pellikka, P.K.E., 2016. The effect of topographic normalization on fractional tree cover mapping in tropical mountains: An assessment based on seasonal Landsat time series. Int. J. Appl. Earth Obs. Geoinf. 52, 20–31.

Beguería, S., Tomas-Burguera, M., Serrano-Notivoli, R., Peña-Angulo, D., Vicente-Serrano, S.M., González-Hidalgo, J.-C., 2019. Gap filling of monthly temperature data and its effect on climatic variability and trends. J. Clim. 32, 7797–7821.

Beygelzimer, A., Kakadet, S., Langford, J., Arya, S., Mount, D., Li, S., Li, M.S., 2015. Package 'FNN'. Accessed June, 1.

Brooks, E.B., Thomas, V.A., Wynne, R.H., Coulston, J.W., 2012. Fitting the multitemporal curve: a Fourier series approach to the missing data problem in remote sensing analysis. IEEE Trans. Geosci. Remote Sens. 50, 3340–3353.

Chen, J., Jönsson, P., Tamura, M., Gu, Z., Matsushita, B., Eklundh, L., 2004. A simple method for reconstructing a high-quality NDVI time-series data set based on the Savitzky-Golay filter. Remote Sens. Environ. 91, 332–344.

Chen, J., Zhu, X., Vogelmann, J.E., Gao, F., Jin, S., 2011. A simple and effective method for filling gaps in Landsat ETM+ SLC-off images. Remote Sens. Environ. 115, 1053–1064.

Cheng, Q., Shen, H., Zhang, L., Yuan, Q., Zeng, C., 2014. Cloud removal for remotely sensed images by similar pixel replacement guided with a spatio-temporal MRF model. ISPRS J. Photogramm. Remote Sens. 92, 54–68.

Chiu, P.C., Selamat, A., Krejcar, O., 2019. Infilling missing rainfall and runoff data for Sarawak, Malaysia using Gaussian mixture model based K-nearest neighbor imputation. In: Wotawa, F., Friedrich, G., Pill, I., Koitz-Hristov, R., Ali, M., (Eds.), Advances and Trends in Artificial Intelligence. From Theory to Practice (pp. 27-38). Cham: Springer International Publishing.

Cover, T.M., Hart, P.E., 1967. Nearest neighbor pattern classification. IEEE Trans. Inf. Theory 13, 21–27.

Foga, S., Scaramuzza, P.L., Guo, S., Zhu, Z., Dilley Jr, R.D., Beckmann, T., Schmidt, G.L., Dwyer, J.L., Hughes, M.J., Laue, B., 2017. Cloud detection algorithm comparison and validation for operational Landsat data products. Remote Sens. Environ. 194, 379–390.

Gao, F., Masek, J., Schwaller, M., Hall, F., 2006. On the blending of the Landsat and MODIS surface reflectance: Predicting daily Landsat surface reflectance. IEEE Trans. Geosci. Remote Sens. 44, 2207–2218.

Gerber, F., Jong, R.d., Schaepman, M.E., Schaepman-Strub, G., & Furrer, R. (2018). Predicting missing values in spatio-temporal remote sensing data. IEEE Trans. Geosci. Remote Sens., 56, 2841–2853.

Griffiths, P., Linden, S.v.d., Kuemmerle, T., Hostert, P., 2013. A pixel-based landsat compositing algorithm for large area land cover mapping. IEEE J. Selected Topics in Appl. Earth Observations Remote Sens., 6, 2088-2101.

Guo, Y., Wang, C., Lei, S., Yang, J., Zhao, Y., 2020. A framework of spatio-temporal fusion algorithm selection for landsat NDVI time series construction. ISPRS Int. J. Geo-Inf. 9, 665.

Heiskanen, J., Adhikari, H., Piiroinen, R., Packalen, P., Pellikka, P.K.E., 2019. Do airborne laser scanning biomass prediction models benefit from Landsat time series, hyperspectral data or forest classification in tropical mosaic landscapes? Int. J. Appl. Earth Obs. Geoinf. 81, 176–185.

Jonsson, P., Eklundh, L., 2002. Seasonality extraction by function fitting to time-series of satellite sensor data. IEEE Trans. Geosci. Remote Sens. 40, 1824–1832.

Ju, J., Roy, D.P., 2008. The availability of cloud-free Landsat ETM+ data over the conterminous United States and globally. Remote Sens. Environ. 112, 1196–1211.

Keller, J.M., Gray, M.R., Givens, J.A., 1985. A fuzzy K-nearest neighbor algorithm. IEEE Trans. Syst., Man, Cybernetics SMC-15, 580–585.

Knorn, J., Rabe, A., Radeloff, V.C., Kuemmerle, T., Kozak, J., Hostert, P., 2009. Land cover mapping of large areas using chain classification of neighboring Landsat satellite images. Remote Sens. Environ. 113, 957–964.

Li, X., Shen, H., Zhang, L., Li, H., 2015. Sparse-based reconstruction of missing information in remote sensing images from spectral/temporal complementary information. ISPRS J. Photogramm. Remote Sens. 106, 1–15.

Luo, Y., Guan, K., Peng, J., 2018. STAIR: A generic and fully-automated method to fuse multiple sources of optical satellite data to generate a high-resolution, daily and cloud-/gap-free surface reflectance product. Remote Sens. Environ. 214, 87–99.

Malambo, L., Heatwole, C.D., 2016. A multitemporal profile-based interpolation method for gap filling nonstationary data. IEEE Trans. Geosci. Remote Sens. 54, 252–261.

Maltamo, M., Kangas, A., 1998. Methods based on k-nearest neighbor regression in the prediction of basal area diameter distribution. Can. J. For. Res. 28, 1107–1115.

Moreno-Martínez, Á., Izquierdo-Verdiguier, E., Maneta, M.P., Camps-Valls, G., Robinson, N., Muñoz-Marí, J., Sedano, F., Clinton, N., Running, S.W., 2020. Multispectral high resolution sensor fusion for smoothing and gap-filling in the cloud. Remote Sens. Environ. 247, 111901.

Pellikka, P.K.E., Heikinheimo, V., Hietanen, J., Schäfer, E., Siljander, M., Heiskanen, J., 2018. Impact of land cover change on aboveground carbon stocks in Afromontane landscape in Kenya. Appl. Geogr. 94, 178–189.

Phiri, D., Morgenroth, J., 2017. Developments in landsat land cover classification methods: a review. Remote Sens. 9, 967.

Pohl, C., Van Genderen, J.L., 1998. Review article multisensor image fusion in remote sensing: concepts, methods and applications. Int. J. Remote Sens. 19, 823–854.

Potapov, P.V., Turubanova, S.A., Hansen, M.C., Adusei, B., Broich, M., Altstatt, A., Mane, L., Justice, C.O., 2012. Quantifying forest cover loss in Democratic Republic of the Congo, 2000–2010, with Landsat ETM+ data. Remote Sens. Environ. 122, 106–116.

Poyatos, R., Sus, O., Badiella, L., Mencuccini, M., Martínez-Vilalta, J., 2018. Gap-filling a spatially explicit plant trait database: comparing imputation methods and different levels of environmental information. Biogeosciences 15, 2601.

Roy, D.P., Ju, J., Kline, K., Scaramuzza, P.L., Kovalskyy, V., Hansen, M., Loveland, T.R., Vermote, E., Zhang, C., 2010. Web-enabled Landsat Data (WELD): Landsat ETM+ composited mosaics of the conterminous United States. Remote Sens. Environ. 114, 35–49.

Roy, D.P., Ju, J., Lewis, P., Schaaf, C., Gao, F., Hansen, M., Lindquist, E., 2008. Multi-temporal MODIS–Landsat data fusion for relative radiometric normalization, gap filling, and prediction of Landsat data. Remote Sens. Environ. 112, 3112–3130.

R Core Team, 2018. R: A language and environment for statistical computing. R Foundation for Statistical Computing, Vienna, Austria.

Shen, H., Li, X., Cheng, Q., Zeng, C., Yang, G., Li, H., Zhang, L., 2015. Missing information reconstruction of remote sensing data: a technical review. IEEE Geosci. Remote Sens. Mag. 3, 61–85.

Vuolo, F., Ng, W.-T., Atzberger, C., 2017. Smoothing and gap-filling of high resolution multi-spectral time series: Example of Landsat data. Int. J. Appl. Earth Obs. Geoinf. 57, 202–213.

White, J.C., Wulder, M.A., Hobart, G.W., Luther, J.E., Hermosilla, T., Griffiths, P., Coops, N.C., Hall, R.J., Hostert, P., Dyk, A., Guindon, L., 2014. Pixel-based image compositing for large-area dense time series applications and science. Canadian Journal of Remote Sensing 40, 192–212.

Wu, W., Ge, L., Luo, J., Huan, R., Yang, Y., 2018. A spectral-temporal patch-based missing area reconstruction for time-series images. Remote Sens. 10.

Wulder, M.A., Loveland, T.R., Roy, D.P., Crawford, C.J., Masek, J.G., Woodcock, C.E., Allen, R.G., Anderson, M.C., Belward, A.S., Cohen, W.B., Dwyer, J., Erb, A., Gao, F., Griffiths, P., Helder, D., Hermosilla, T., Hipple, J.D., Hostert, P., Hughes, M.J., Huntington, J., Johnson, D.M., Kennedy, R., Kilic, A., Li, Z., Lymburner, L., McCorkel, J., Pahlevan, N., Scambos, T.A., Schaaf, C., Schott, J.R., Sheng, Y., Storey, J., Vermote, E., Vogelmann, J., White, J.C., Wynne, R.H., Zhu, Z., 2019. Current status of Landsat program, science, and applications. Remote Sens. Environ. 225, 127–147.

Xing, C., Chen, N., Zhang, X., Gong, J., 2017. A machine learning based reconstruction method for satellite remote sensing of soil moisture images with in situ observations. Remote Sens. 9, 484.

Yan, L., Roy, D.P., 2020. Spatially and temporally complete Landsat reflectance time series modelling: The fill-and-fit approach. Remote Sens. Environ. 241, 111718.

Yan, L., Roy, P.D., 2018. Large-area gap filling of landsat reflectance time series by spectral-angle-mapper based spatio-temporal similarity (SAMSTS). Remote Sens. 10, 609.

Zhang, C., Li, W., Travis, D., 2007. Gaps-fill of SLC-off Landsat ETM+ satellite image using a geostatistical approach. Int. J. Remote Sens. 28, 5103–5122.

Zhang, J., 2010. Multi-source remote sensing data fusion: status and trends. Int. J. Image Data Fusion 1, 5–24.

Zhou, F., Zhong, D., 2020. Kalman filter method for generating time-series synthetic Landsat images and their uncertainty from Landsat and MODIS observations. Remote Sens. Environ. 239, 111628.

Zhu, X., Chen, J., Gao, F., Chen, X., Masek, J.G., 2010. An enhanced spatial and temporal adaptive reflectance fusion model for complex heterogeneous regions. Remote Sens. Environ. 114, 2610–2623.

Zhu, X., Liu, D., Chen, J., 2012. A new geostatistical approach for filling gaps in Landsat ETM+ SLC-off images. Remote Sens. Environ. 124, 49–60.

Zhu, Z., Woodcock, C.E., 2014. Continuous change detection and classification of land cover using all available Landsat data. Remote Sens. Environ. 144, 152–171.

Zhu, Z., Wulder, M.A., Roy, D.P., Woodcock, C.E., Hansen, M.C., Radeloff, V.C., Healey, S.P., Schaaf, C., Hostert, P., Strobl, P., Pekel, J.-F., Lymburner, L., Pahlevan, N., Scambos, T.A., 2019. Benefits of the free and open Landsat data policy. Remote Sens. Environ. 224, 382–385.